Non-Destructive Characterization of Magnetic Polymeric Scaffolds using Terahertz Time-of-Flight Imaging

Sonia Zappia, Rosa Scapaticci, *Member, IEEE*, Matteo Bruno Lodi, *Member, IEEE*, Alessandro Fanti, *Senior Member, IEEE*, Giuseppe Ruello, *Senior Member, IEEE*, Lorenzo Crocco, *Senior Member, IEEE*, Ilaria Catapano, *Member, IEEE*

***Abstract*—Magnetic Scaffolds MagS are 3D composite materials, in which magnetic nanoparticles (MNPs) are used to load a polymeric matrix. Due to their wide use in various medical applications, there is an increasing demand of advanced techniques for non-destructive quality assessment procedures aimed at verifying the absence of defects and, more generally, dedicated to the characterization of MagS. In this framework, the use of TeraHertz (THz) waves for the non-destructive characterization of multifunctional scaffolds represents an open challenge for the scientific community. This paper deals with an approach for the characterization of MagS by means of a THz time-domain system used in reflection mode. THz analyses are performed on poly(ϵ - capprolactone) (PCL) scaffolds magnetized with iron oxide (Fe_3O_4) MNPs through a drop-casting deposition and tuned to obtain different distributions of MNP in the biomaterial. The proposed data processing approach allows a quantitative characterization MagS, in terms of their (estimated) thickness and refractive index. Moreover, the proposed procedure allows to identify the areas of the scaffold wherein MNP are mainly concentrated and thus, it gives us information about MNP spatial distribution.**

***Index Terms*—THz Imaging, Composite materials, Magnetic Nanoparticles, Non-destructive inspection.**

I. Introduction

COMPOSITE materials are a combination of two or more materials that differ in terms of chemical or physical properties and are merged to create a new material having a separate and distinct final structure [1]–[4]. Polymer-based composite materials have emerged as an interesting alternative to other materials (i.e., metals, plastics and ceramics) in several applications, thanks to their mechanical properties, flexibility and structural integrity [5]. However, it is worth noticing that the physical and chemical manufacturing routes of composite materials are complex [6]–[8]. In this regard, it is ever-increasing the demand for effective, possibly non-destructive procedures for quality assessment [5]. Among composite materials, magnetic polymer-based scaffolds raised a huge interest due to their wide use in several medical applications such as cancer therapy [9], tissue engineering [10] and drug delivery [11]. A magnetic scaffold MagS can be obtained by physical loading of magnetic nanoparticles (MNPs) into a polymeric matrix to obtain a multifunctional and theranostic device [12]–[14]. The advantage of MagS is that they can be controlled using an external magnetic field, which makes them appealing for applications in which the scaffold must be implanted in vivo, such as tissue repair [15]. Furthermore, MagS can target and control the delivery of soluble factors, such as growth factors, hormones, and peptides directly to the implantation site under the magnetic field to improve the fixation and stability of implant [16] and has good mechanical properties [17] and excellent biocompatibility [18]. However the production process of the MagS is often associated to a non uniform final spatial distribution of MNPs in the polymeric matrix [19], so that recent and intense progresses on the manufacturing strategies are ongoing. The potential of MagS and the need to control the quality of their productive process motivate the development of procedures for routine and reproducible non destructive characterization of MNP distribution in the polymeric matrix.

Currently, several methods are exploited to analyze MagS such as Micro-Computed Tomography (MicroCTs) [20], [21], Scanning Electron Microscope (SEM) [22]–[24], and Transmission Electron Microscopy (TEM) [22], [25], [26] and each one of them has its advantages and drawbacks.

MicroCT uses X-rays to capture the image and, hence, shape and size of the polymer and nanocomposite fibers [20], [21]. The images obtained through the Micro-CT system scan allows for the 3D reconstruction of the nanocomposite fibers and, hence, the distribution of MNPs along the fibers [20]. X-rays system, provide high resolution images but have the disadvantage of using ionizing radiations, always related to risks involving the operator, as well as the material itself that could be damaged [27].

SEM uses a focused beam of high-energy electrons to generate a variety of signals at the surface of solid specimens. The signals derived from electron-sample interactions reveal information about the sample including surface morphology (texture). The shape and the porosity of magnetic scaffolds were observed by SEM images in several works available in literature [22]–[24], [28]. However, SEMs are expensive and must be housed in an area free of any possible electric, magnetic or vibration interference. Also, to investigate the

S. Zappia, R. Scapaticci, L. Crocco and I. Catapano are with the Institute for Electromagnetic Sensing of the Environment, National Research Council of Italy, 80124 Naples, Italy (corresponding e-mail: catapano.i@irea.cnr.it).

M. B. Lodi and A. Fanti are with the Department of Electrical and Electronic Engineering, University of Cagliari, via Marengo 2, 09123, Cagliari, Italy (corresponding e-mail: alessandro.fanti@diee.unica.it).

Giuseppe Ruello is with the Department of Electrical Engineering and Information Technology (DIETI) University of Naples "Federico II" - Via Claudio 21,80125 Naples, Italy (corresponding e-mail: giuseppe.ruello@unina.it).

sample in depth, slicing and destructive preparation are needed [29].

TEM is a microscopy technique in which a beam of electrons is transmitted through the sample under test to form an image. The image is derived from the interaction of the electrons with the sample as the beam is transmitted through it. TEMs provide topographical, morphological, compositional and crystalline information. The images allow researchers to view samples at a molecular level, making it possible to analyze structure and texture [30]. This type of technique has been used to explore the morphology of the MNPs distributed along the fibers of the scaffolds [22], [25], [26]. However, to obtain a TEM image, samples must be sliced thin enough for electrons to pass through (i.e., usually the specimens has an ultrathin section less than 100 nm). Therefore, non destructive evaluation is not possible. Moreover, the specimens must be prepared as a thin foil, or etched to be thin enough for the beam to penetrate. Constraints make the sample preparation laborious. Furthermore, other disadvantages are that TEM systems are large and very expensive and their operation and analysis requires special training [29].

Thanks to its unique properties, TeraHertz (THz) imaging may represent a potential candidate for MagS non destructive characterization. THz are electromagnetic (EM) waves ranging from 0.1 to 10 THz (wavelength from 3 mm to 30 μm), which are able to penetrate a wide range of non-conducting materials, e.g., plastics, polymers, ceramics, wood, and glass [31], just to name a few. THz waves are non ionizing, thus allowing non-destructive inspection of the materials without requiring specific security protocols. Various applications of THz waves have been reported in many fields, including medical diagnosis [32], pharmaceutical analysis [33], security enhancement [34], cultural heritage [35], and food quality control [36]. However, THz waves are strongly attenuated by water and suffer from the environmental conditions, such as humidity [37].

One of the most promising applications of THz technologies [38] is the non-destructive evaluation of composite materials [37], [39]–[46]. In particular, a number of efforts have been dedicated to non-destructive evaluation of polymeric (dielectric) scaffolds [47]–[49]. THz technology has been exploited for the detection of damages such as non-impregnated areas in polymer composite materials [37], [50], [51], or for the evaluation of the porosity of the polymeric matrix [5]. Considering the above framework, this paper presents a method for the non destructive characterization of MagS and the determination of the distribution of MNP in the polymer matrix, using THz technology. It is worth noting that although THz technology is well known for the non-destructive testing of composite materials, to the best of the authors' knowledge its application to MagS is a new challenge that has not yet been thoroughly investigated by the scientific community. This paper describes the procedure used in [52], [53], [54], where THz imaging was applied to MagS for the first time. A measurement protocol is developed for the quantitative characterization of MagS, allowing estimation of thickness (Δ) and refractive index (η). The 2D distribution of MNPs in the MagS is determined using an ad-hoc procedure based on the analysis of THz data collected during the experiments and the use of reference time-of-flight values calculated considering homogeneous ideal scaffolds. In order to characterize the spatial distribution of the MNPs two indices are introduced: 1) the Magnetization Index (I_m), which accounts for the amount of MNP in the scaffolds; 2) the Magnetization Distribution Index (I_{md}), which takes into account the areas where MNP are more concentrated (with respect to a homogeneous distribution of MNP in the scaffold). 2D maps are presented to visually detect the presence of MNP in MagS and to identify the areas where MNP are most concentrated and their distribution in the polymer matrix.

The work is structured as follows: Sec. II introduces the general concept of MagS with a specific focus on our case studies, Sec. III describes the time-of-flight (ToF) sensing principle, the measurement system, the data filtering used, and the measurement protocol applied to the laboratory case studies. Sec. IV is devoted to describe the strategy adopted to determine the thickness, the refractive index and the MNPs spatial distribution of MagS. In Sec. V the results are presented. Finally, the discussion and the conclusions follow in Sec. VI and Sec. VII, respectively.

II. Materials

A. Magnetic Scaffolds

MagS are 3D composite materials, in which iron oxide (Fe_3O_4) MNPs are used to load a polymeric matrix made of poly(ϵ - capprolactone) (PCL).

It is well known that polymer scaffolds used for tissue engineering should possess proper architecture and mechanical properties to support cell adhesion, proliferation, and differentiation [55]. Typical scaffold designs have included meshes and fibers; these designs are chosen because they promote uniform cell distribution, diffusion of nutrients, and the growth of organized cell communities [56]. Therefore, the architecture of a PCL scaffold is made using fibers that are superimposed on each other forming a grid to obtain a solid structure having a certain porosity. The choice of the ideal fiber size and the porosity of the scaffold depends on the proposed function of the scaffold itself [57].

Regarding the process of incorporation of MNP into the polymer matrix, the one used for the analyzed MagS consists of dropping the MNP dispersed in water onto the PCL scaffolds and the deposition occurs under the driving force of an external magnet [52].

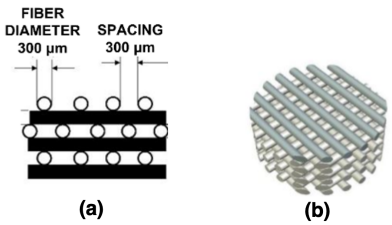

Fig. 1. a) 3D-Insert consisting of a 90°-interlaced fiber architecture, with a fiber diameter of 300 μm, spaced by 300 μm. b) Image of the 3D structure of the scaffold.

B. Laboratory case studies

Polymeric scaffolds produced by 3D Biotek (3D Biotek LLC) have been considered in this study. The set of 3D-Insert are constituted by a $90°$-interlaced fiber architecture, with a fiber diameter of 300 μm, spaced by 300 μm, resulting in a nominal porosity of about 80% (see Fig. 1a). These standard poly-caprolactone (PCL) disks have a 5 mm diameter. A representative image of the 3D structure of the scaffold is shown in Fig. 1b. The drop-casting deposition is tuned to obtain different distributions of MNPs in the biomaterial as described in [52]. The four MagS analyzed in this study are shown in Fig. 2, where the sample named $0A$ does not contain MNPs and is used as reference.

III. Methods

A. Sensing Principle of the measures

THz pulsed imaging (TPI) also known as THz ToF imaging has the unique property of providing a 3D map of the object under test by exploiting THz data collected in reflection mode [58]. This technique was used for the first time by Mittleman and coworkers to produce the internal structure of a 3.5 inch floppy disk [59]. In brief, the object is probed by a pulsed signal and the reflected waveform is collected as a time-dependent function within a certain observation time window using a THz Time Domain System (TDS) configuration.

By plotting the gathered waveform referred to a measurement point, a trace showing the amplitude-time of the reflected signal over the target (called A-scan) is obtained, which accounts for the reflection from the object surface and its inner EM features (if the object is non-metallic) [60] (see Fig. 3). The vertical axis of the A-scan represents the amplitude of the signal, the horizontal axis is the time axis and represents the ToF, that is, the time *t* that the waveform employs to propagate from the emitter to an EM discontinuity and to go back to the receiver. The time of flight *t* is related to the distance *d* between THz probes and the detected discontinuities as:

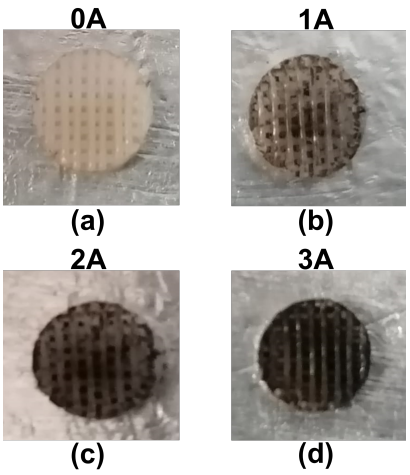

Fig. 2. Photos of the samples: (a) scaffold without MNPs named sample 0A; (b)-(d) scaffolds with a different amount of MNPs and referred as sample 1A, 2A and 3A, respectively.

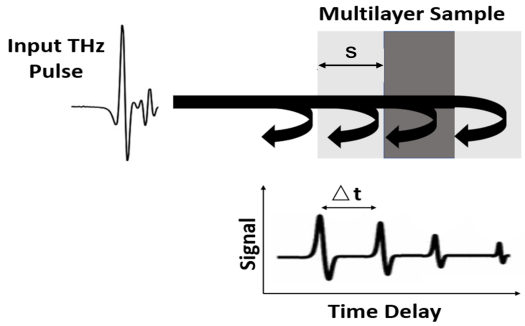

Fig. 3. Time of flight sensing principle: probing THz pulse (left upper panel); pulse interaction with a multilayer sample (right upper panel); collected THz signal due to the multilayer sample (lower panel).

$$t = \frac{2d}{v} \tag{1}$$

v being the EM wave propagation velocity into the object.

It is worth to pointing out that, starting from the measured signals, several THz images can be generated, each one revealing a different feature of the analyzed sample. For example, an image obtained by plotting the temporal position of the first peak of the gathered waveforms at each measurement point, reveals differences in the refractive index and the surface tomography of the sample [61]. Furthermore, by plotting, pixel by pixel, the signal amplitude occurring in a specific time window, a THz false color image is derived, which accounts for the inner features of the object.

The effectiveness of THz imaging and, more generally, of EM diagnostics benefits from a data processing tool aimed at improving the imaging performance of the hardware device. In fact, undesired signals, like noise and clutter, corrupt the useful data and thus the imaging capabilities. Therefore, data filtering procedures are useful to reduce noise and clutter and improve the imaging results.

B. Measurement System and Filtering Procedure

THz data have been collected by means of the Fiber Coupled THz Time Domain (FiCO), shown in Fig. 4. The system consists of three main components: a) the FiCO base unit; b) emitter and receiver heads; c) the laser source. The laser source is a free space pulsed laser working at 1560 nm with average power higher than 200 mW and it acts as primary source. The laser signal is driven into FiCO base unit by means of two steering mirrors. The FiCO base unit splits the input signal into a pump and probe beam used to generate THz waves and it is connected the emitter and receiver heads by means of fiber optic cables. The system collects data in the useful frequency range from 80 GHz up to 3 THz (lower and higher frequency signal components are overlapped by noise) and the estimated THz beam size at the focal point is about 1 mm. The system is equipped with an ad hoc designed imaging module, which allows measurements in normal reflection mode. In particular, the object under test is positioned on a movable platform, which automatically scans

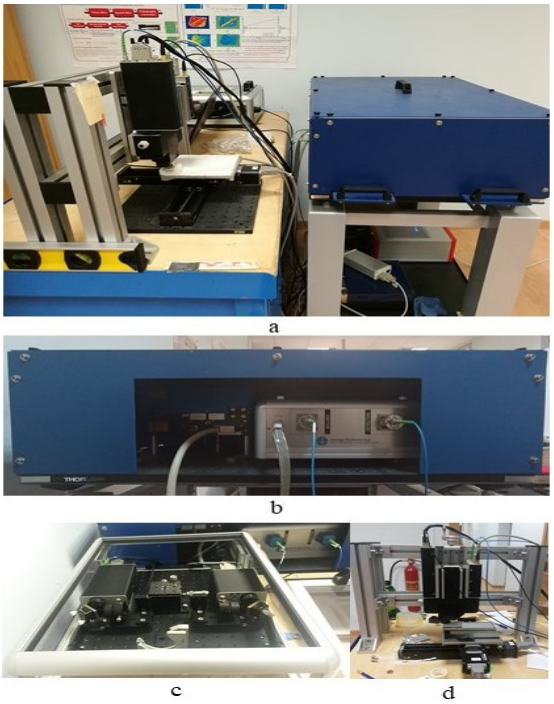

Fig. 4. Zomega Fico system: (a) global view; (b) primary laser source and optical delay line; (c) purge chamber; (d) imaging module.

a 150 mm ×150 mm area with a minimum spatial offset of 0.12 mm, and it is located at the focal distance by manually adjusting the height of the THz normal reflection module. 3D data (2D in space + 1D in time) are collected within a 100 ps observation time window. The waveform acquisition speed can be up to 500 Hz, and the maximum dynamic range (DNR) is 30 dB, while the typical DNR is 20 dB. The data can be visualized and processed after the measurement stage.

Concerning data processing, an ad-hoc strategy has been designed in order to filter data and visualize THz images. This strategy involves two different steps in time-domain aimed at reducing noise and filtering out undesired signal introduced by the adopted THz system, as shown in the flow chart in Fig. 5. The first step aims at removing the undesired low and high frequency signal components and it is made up of a Frequency Band Pass Filter (BPF) procedure selecting the signal components in the range 80 GHz - 3 THz. The second step is a noise filtering procedure based on the Singular Value Decomposition (SVD) of the band pass filtered data matrix. The SVD data filtering procedure, which is detailed in [35], filters the noise out, while preserves the image details, by using a suitable threshold T_{svd}. A good choice is to set T_{svd} in such way that the energy of the filtered data matrix is about the $90 - 95\%$ of the energy of the collected data matrix [62]. In

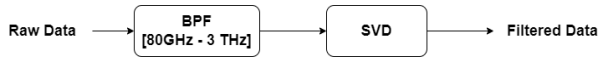

Fig. 5. Signal Filtering Procedure: Step 1 - Band Pass Filter (BPF); Step 2 – Filtering procedure based on the data matrix Singular Value Decomposition (SVD).

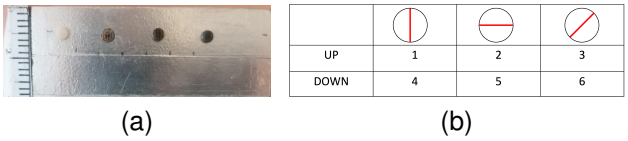

Fig. 6. a) Samples placed on a metal plate. b) Measurement set up; we will refer to the six configurations with numbers from 1 to 6.

the case of THz imaging, as shown in [35], is observed that, the singular spectrum of a generic data matrix is characterized by a fast decay followed by a smooth (almost constant) behavior of the singular values. Accordingly, T_{svd} is chosen as the index of the singular value in correspondence of the point where the spectrum changes its slope, i.e., the index of the singular value where the fast decay of the singular values is followed by the smooth one.

C. Measurement Protocol

The procedure used to carry out the measurements of the Samples under Test (SuT) can be summarized in the following steps.

1) The samples are placed on a metal plate in order to have a unique temporal and spatial reference (see Fig 6a). This choice is useful because the metal totally reflects the signal passing through the sample allowing us to identify the time corresponding to the last peak of the gathered waveforms, due to sample-metal interface (end of the specimens).
2) Six measures are made for each SuT that are numbered from one to six and summarized in Fig. 6b. The samples are analyzed by collecting data on both sides (up and down) and with three different fibers orientations (see Fig. 7). In particular, the specimens are measured with the fibers oriented as shown in Fig 7a (the starting position $\alpha = 0°$, where α is the angle between the fiber shown in red in Fig. 7 and the y axis), rotated by $45°$ ($\alpha = 45°$, see Fig. 7b) and by $90°$ ($\alpha = 90°$, Fig. 7c), with respect to the initial position.

The measurement protocol consists of six measures for each SuT and this is made because small variations in the results may occur, mainly due to two factors. The first one is the random placement of the sample on the scanning platform of the THz measurement system. The second one is the texture of

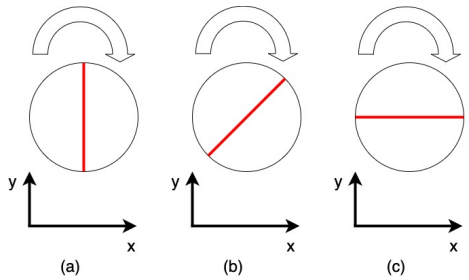

Fig. 7. Different fibers orientations used to carry out the measurement. a) Starting position $\alpha = 0°$. b) Rotaded by $45°$. c) Rotaded by $90°$.

the sample, which consists of $90°$ -interlaced fiber architecture, as described in Sec. II-B, that can affect the propagation time of the THz signal within the object. The polymer matrix, as shown in Fig. 1, has empty spaces between the fibres, which alters the propagation of the THz signal. Furthermore, the time that the THz signal employs to propagate depends on the mutual position of the fibres, and thus on their orientation with respect to the emitter and the receiver locations.

THz measurements were performed in uncontrolled environment conditions with temperature values in the range 28°C - 30°C and humidity percentages from 30% to 35%. The data were gathered by scanning a 10 mm x 10 mm area with a 0.12 mm spatial offset along x and y axes, which was selected in agreement with the spatial variability of the geometrical features of the investigated samples. The time required to collect each data set was less than 5 minutes, while the processing time was about a couple of minutes. Of course, such a time is not negligible but, in our opinion, is reasonable for high precision laboratory measurements.

Moreover, the thickness of the samples in Fig. 2, say d_m, are shown in Tab I. Such values were measured by means of a manual gauge, having an accuracy of about 10^{-1} mm.

TABLE I
THICKNESS OF THE MAGS.

Sample	$0A$	$1A$	$2A$	$3A$
$d_m[mm]$	1.55	1.40	1.50	1.30

Thickness of the magnetic scaffolds, d_m, measured with a manual gauge

IV. CHARACTERIZATION OF THE MAGS

This section is devoted to describe the approach to characterized the MagS, which can be summarized in the following steps:

- Estimation of the thickness (Δ);
- Estimation of the refractive index (η);
- Evaluation of the 2D spatial distribution of the MNPs (MDM);
  - Definition of THz Propagation Delay Map (PDM);
  - Definition of the Magnetization Index (I_m);
  - Definition of THz reference propagation times (t_M, t_{NM});
  - Definition of Magnetization Concentration Mask (MCM);
  - Definition of the Magnetization Distribution Index (I_{md});

The approach is applied to the filtered THz data obtained as described in Sec. III-B. All THz data processing is done with Matlab codes.

A. Thickness Estimation

The thickness of the SuT (Δ, in mm), is computed by using the ToF formula, see Eq. 1. In particular, it is estimated as the difference between the distance from the emitter/receiver to the metallic surface on which the samples are placed, say d_1, and the distance between the emitter/receiver and the sample surface, i.e., the top of the scaffold, say d_2 (see Fig. 8). The distances d_1 and d_2 are computed according to the ToF formula (1):

$$d_i = \frac{c \cdot t_i}{2} \tag{2}$$

with $i = 1, 2$; where c is the speed of light in the vacuum (m/s) and t_i is the time, in ps, that the waveform employs to propagate from the emitter to the metal plate (t_1) or to the top of the scaffold (t_2) and go back to the receiver.

The time t_1 has been estimated from the A-Scan obtained by averaging the collected waveforms referred to the parts of scanned area that are not covered by the scaffold and it is referred to as external area (see Fig. 9a). This A-Scan takes into account the waveforms collected outside the sample, and t_1 is identified as the first minimum, calculated going back in time, starting from the peak of the reflected signal due to air-metal interface (see Fig. 9b).

The time t_2 is estimated from the A-Scan obtained by averaging the collected waveforms of the scanned area intercepting the scaffold, and referred to as internal area (see Fig. 9a). In particular, t_2 is identified as the first minimum value, just before the peak due to air-sample interface, see Fig. 9c.

Once the two distances have been estimated, it is possible to estimate the thickness of the scaffold by simply subtracting $\Delta = d_1 - d_2$.

B. Refractive Index Estimation

The second step involves the identification of the refractive index (η) of the analyzed samples and allows the characterization of the SuT from an EM point of view. Considering that MagS is not homogeneous, by the term refractive index we mean the effective refractive index. This value, once again, is derived from the ToF formula (1). Let v be the EM wave propagation velocity into the object, it is given by $v = \frac{c}{\eta}$. Hence, the refractive index η is derived as :

$$\eta = \frac{c \cdot t_4}{2 \cdot \Delta} \tag{3}$$

where Δ is the estimated thickness of the object and t_4 represents the time that the waveform employs to propagate within the SuT. This time is given by the difference between the time instant t_3 corresponding to the peak of the reflected wave due to the object-metal interface and the time instant t_2 corresponding to the peak referred to top face of the scaffold

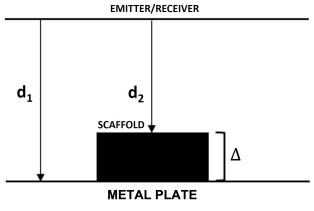

Fig. 8. d_1 is the distance between the emitter/receiver and the metal plate. d_2 is the distance between the emitter/receiver and the surface of the scaffold. Δ is the thickness of the object.

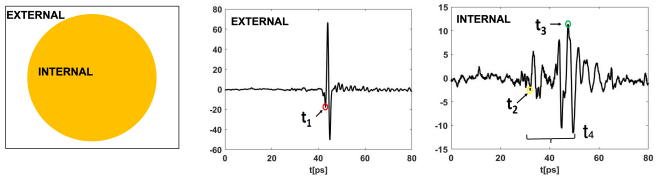

Fig. 9. a) Scan Area: external and internal points exploited to derive the averaged A- scans. The yellow circle represents the scaffold. b) Averaged A Scan from which the value of t_1, highlighted by a red circle, is derived. c) Averaged A Scan used to derive the value of t_2 and t_3 pointed out by a yellow circle and a green one, respectively. t_4 represents the time that the waveform employs to propagate within the SuT.

(see Fig. 9c).

C. MNPs Spatial Distribution Estimation

To extract the spatial distribution of MNPs in the polymeric matrix, the THz Propagation Delay Map (PDM) of the SuT is first derived. PDM is a 2D image representing the propagation time delay of the THz wave due to the presence of MNPs into the scaffold. Such map is a 2D differential image obtained by subtracting, for each pixel, the propagation time referred to the sample under test and a reference propagation time (t_{NM}) computed by considering an ideal homogeneous scaffold having the same thickness of the surveyed one but being without MNPs. The propagation time referred to the SuT is retrieved from the measured data, for each pixel of the scanned area intercepting the scaffold, as the value of the time interval occurring between the time instant of the peak due to the scaffold top face (air-scaffold interface), and the time instant of the peak due to the scaffold bottom face (scaffold-metal plate interface). Of course, the duration of this time range depends on the material wherein the signal propagation occurs and it is, therefore, affected by the presence and the amount of MNPs. The reference propagation time (t_{NM}) is the propagation time referred to a scaffold having the same thickness of the scaffold under test and the refractive index estimated for the sample $0A$ in Fig. 2, i.e., the scaffold without MNPs. Then, the pixels of the scaffold wherein there are MNPs are detected from the PDM as the ones different from zero. The PDM allows the estimate of a Magnetization Index (I_m), synthetically encoding the amount of MNPs present in the SuT (with respect to a homogeneous reference). The I_m value is given by the ratio between the number of pixels containing MNPs and the total number of pixels discretizing the scanning area and intercepting the scaffold, i.e. the number P of pixels belonging to the internal area (see Fig. 9a);

$$I_m = \frac{\sum_{i,j=1}^{N,M}(x_{i,j} > 0)}{P} \tag{4}$$

being $x_{i,j}$ the pixel considering and $N \times M$ the dimension of the image.

Furthermore, the areas where the MNP are mainly concentrated are retrieved by introducing a threshold T defined by the difference between the times of flight of the reference scaffold without MNPs (t_{NM}) and the time of flight for the one homogeneously loaded with MNPs (t_M). This latter is derived using the ToF formula (Eq. 1) where Δ is the thickness of the SuT and v is the EM wave velocity in an object having the refractive index η estimated for the SuT. The value T is used to threshold the PDM and to obtain a binary magnetization map, which we will refer to as Magnetization Concentration Mask (MCM). In this map, the pixels where the propagation time is larger than T are set to one, being estimated as the pixel where the presence of the MNPs significantly affects the THz signal propagation through the sample. The MCM allows the estimate of a Magnetization Distribution Index (I_{md}), which accounts for the areas of the scaffolds where the MNPs are mostly concentrated (with respect to a homogeneous distribution of MNPs in the polymeric matrix). The I_{md} value has been calculated as the ratio between the number of pixels where the propagation time is larger than T and the total number of pixels P:

$$I_{md} = \frac{\sum_{i,j=1}^{N,M}(x_{i,j} > T)}{P} \tag{5}$$

being $x_{i,j}$, N and M defined as above.

Finally, the 2D MNPs Distribution Map (MDM) is retrived by multiplying pixel by pixel the binary MCM and the map of the filtered THz signal amplitude (i.e., THz False colors image). This image is normalized to its maximum value and allows to distinguish the areas of the SuT where MNPs are mostly concentrated and to detect how the distribution of the MNPs changes along x and y directions.

V. THz Results of the Case Studies

The results obtained for the MagS introduced in Sec. II-B (Fig. 2) using the procedures detailed in Sec. IV are reported in this section.

Tab. II shows the time t_1, and the values t_2 and t_3, derived from the A-scans described in Sec. IV-A and IV-B, for the six measurement set up (see Fig. 6b). These values were used to derive the thickness Δ and refractive index η shown in Tab. III, for measurement 1 to 6. In addition, for each sample the results of Δ and η were averaged: 1) M_{up} contains the average values of measurements 1-2-3 (i.e., sample upwards with three different fibre orientations: $\alpha = 0°$, $90°$, $45°$); 2) M_{down} contains the average of measurements 4-5-6 (i.e., sample downwards with three different fibre orientations: $\alpha = 0°$, $90°$, $45°$); 3) M_{tot} contains the average of all six measurements. Table IV compares the average thickness values derived from THz data (Δ), referred to all the six measurements (M_{tot}), with those measured by means of a manual gauge (d_m), having an accuracy of about 10^{-1} mm. Table V shows at its first row the THz propagation times of the reference samples without MNPs (t_{NM}) exploited to derive the PDMs in Fig. 10, referring to the sample $1A$, $2A$ and $3A$.

The second row of Tab. V contains the instant times t_M referred to the scaffolds homogeneously loaded with MNPs, that allow to obtain the threshold T (see the third row of Tab. V) used to retrieve the MCMs shown in Fig. 11b, Fig. 12b

TABLE II

	$t_1[ps]$				$t_2[ps]$				$t_3[ps]$			
Measurement	$0A$	$1A$	$2A$	$3A$	$0A$	$1A$	$2A$	$3A$	$0A$	$1A$	$2A$	$3A$
1	42.9	41.3	42.0	43.7	32.0	31.7	32.1	34.8	48.4	46.9	47.7	49.2
2	43.3	41.4	41.3	41.0	32.6	32.0	31.4	32.1	48.9	46.8	47.1	46.6
3	41.2	41.2	42.1	42.1	30.6	31.5	32.0	33.2	47.0	46.7	47.8	47.4
4	41.6	41.9	42.8	42.5	30.6	32.2	32.8	33.7	47.3	47.2	48.6	48.2
5	43.3	41.4	41.2	42.3	32.7	31.2	31.2	33.5	48.9	46.7	46.8	47.6
6	42.4	41.7	42.4	44.6	31.7	32.0	32.4	35.7	48.2	47.0	48.5	49.8

t_1, t_2 and t_3 in ps for all the measurement set.

TABLE III

	$0A$ **[mm]**		$1A$		$2A$		$3A$	
Measurement	Δ[mm]	η	Δ[mm]	η	Δ[mm]	η	Δ[mm]	η
1	1.62	1.52	1.47	1.56	1.50	1.56	1.34	1.61
2	1.61	1.52	1.41	1.57	1.50	1.58	1.34	1.61
3	1.59	1.54	1.45	1.57	1.50	1.58	1.33	1.60
4	1.65	1.52	1.45	1.55	1.49	1.59	1.32	1.65
5	1.58	1.54	1.45	1.55	1.50	1.57	1.32	1.60
6	1.60	1.55	1.45	1.55	1.51	1.60	1.34	1.58
M_{up}	1.61	1.53	1.44	1.57	1.50	1.57	1.34	1.61
M_{down}	1.61	1.54	1.45	1.55	1.50	1.59	1.33	1.61
M_{tot}	1.61	1.53	1.45	1.56	1.50	1.58	1.33	1.61

Δ and η values for each measurement and their averages M_{up}, M_{down}, M_{tot}.

TABLE IV

Sample	$0A$	$1A$	$2A$	$3A$
$d_m[mm]$	1.55	1.40	1.50	1.30
$\Delta[mm]$	1.61	1.45	1.50	1.33

Thickness of the magnetic scaffolds: d_m is the value measured with a manual gauge - Δ is the averaged thickness estimated for all the measurement set.

TABLE V

Sample	$1A$	$2A$	$3A$
$t_{NM}[ps]$	14.70	15.30	13.56
$t_M[ps]$	15.00	15.80	14.28
$T[ps]$	0.30	0.50	0.72

t_M, t_{NM} and $T[ps]$ calculated considering the average Δ and the average η for all the six measurement set.

TABLE VI

Sample	$0A$	$1A$	$2A$	$3A$
I_m	0	0.88	0.97	0.99
I_{md}	0	0.14	0.27	0.48

I_m and I_{md} for the MagS.

and Fig. 13b. Tab. VI. contains the Magnetization Index (I_m) and the Magnetization Distribution Index (I_{md}).

The 2D MNPs Distribution Map (MDM) are shown in Fig. 11c, Fig. 12c and Fig. 13c compared with the optical image of the corresponding MagS.

VI. Discussion

THz data referred to the six measurement setups shown in Tab. II have been used to estimate Δ and η, and the results are presented in Tab. III.

As shown in Tab. III, small variations in the results occur due to the different position of the MagS texture, which is made by $90°$-shifted highly porous mesh, on the scanning platform of the THz system. The texture of the MagS and the presence of empty spaces between the fibers, affect the propagation time, which depends on the mutual position of the fibers and on their orientation with respect to the emitter and the receiver locations.

There are also small variations in the results of Δ and η, as shown from the row 1 to 6 in Tab. III, due to the fact that such values are computed from the instant times t_1, t_2 and t_3 (see Sec. IV-A and IV-B).

Tab. III shows the estimated values of Δ and η for the single measure (from row 1 to 6) and for the averaged measures. The results do not differ significantly each other if we consider an approximation to the first digit. Therefore, they suggest that a single measurement could be sufficient, even if the

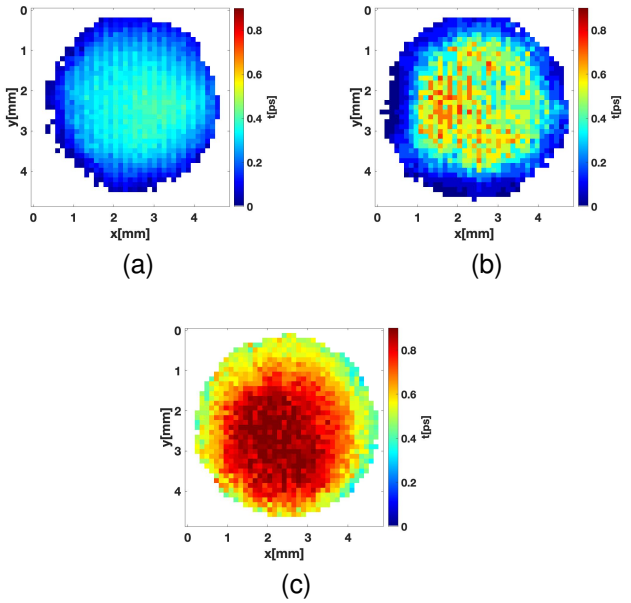

Fig. 10. Propagation Delay Maps (PDMs). a) 1A. b) 2A. c) 3A.

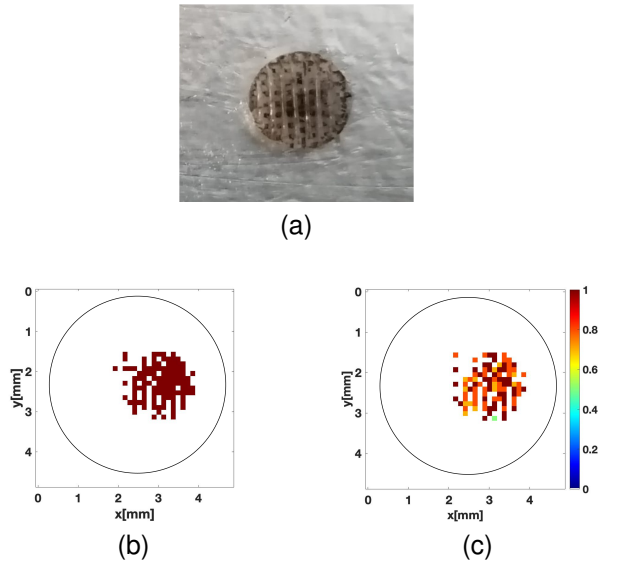

Fig. 11. a) Photograph of the MagS 1A. b) MCM 1A. c) 2D MDM 1A.

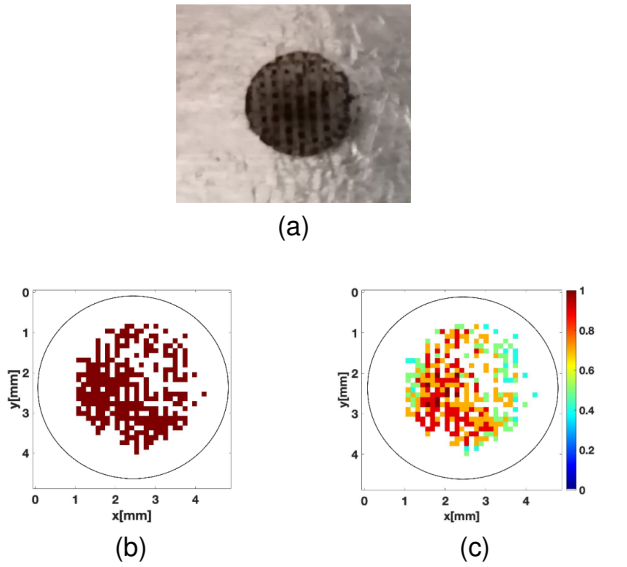

Fig. 12. a) Photograph of the MagS 2A. b) MCM 2A. c) 2D MDM 2A.

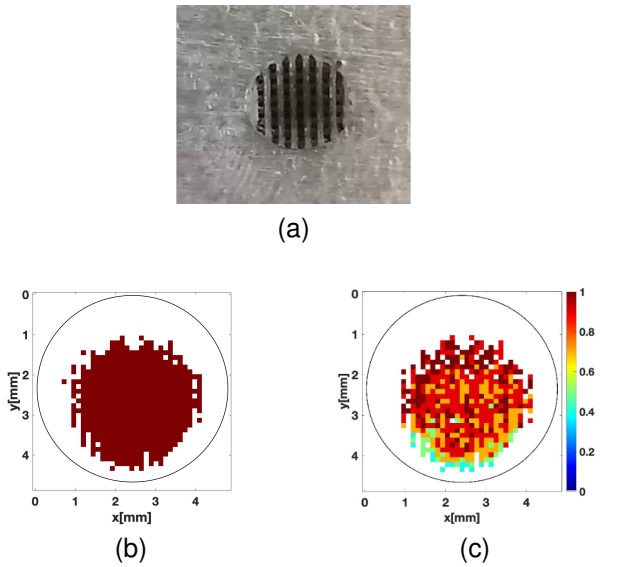

Fig. 13. a) Photograph of the MagS 3A. b) MCM 3A. c) 2D MDM 3A.

average of three measurements, with the sample up or down, or six measurements (i.e., MagS up and down) increases the robustness of the MagS characterization.

The effectiveness of the procedures described in Sec IV-A is demonstrated by comparing the averaged values estimated from the THz data Δ (i.e., referred to M_{tot}), and the values measured with the manual gauge d_m with an accuracy of about 10^{-1} mm. The results in Tab. IV demonstrate that the proposed method gives good results considering the accuracy of the manual gauge. It is worth noting that, as shown in Tab. III, the sample without MNPs (i.e., $0A$) has the lowest η value, as expected, while the other samples show an increasing trend. In particular, sample $3A$ is characterized by the highest η value and this is compliant with the largest amount of MNPs.

The PDMs shown in Fig. 10 contain the THz propagation delay, in ps, introduced by the presence of MNP and allow the introduction of the magnetization indices, I_m, shown in the first row of Tab. VI. The obtained results state, as foreseeable, that when the amount of MNP increases also η increases, while I_m approaches to 1. Moreover, the results referred to I_{md} (see second row of Tab. VI) show that higher I_{md} values correspond to larger areas where MNPs are concentrated, which is confirmed by both the MCM and the picture of the MagS.

Looking at the photo of sample $1A$ in Fig. 11a, it is possible to note that there is a higher MNP concentration in the center, as confirmed by the MCM in Fig. 11b. Similarly, for the sample $2A$, the MNPs are present in lower amounts at the edges, while they are present in higher amounts in the other parts of the scaffolds, as shown in the photo of the specimen

in Fig 12a and confirmed by the MCM (see Fig. 12b). Finally, sample $3A$ appears to have a higher MNP concentration, as confirmed both by the photography in Fig. 13a as well as by our results in Fig. 13b

The 2D maps of MNP distribution in Fig. 11c, Fig. 12c and Fig. 13c, each normalized to its maximum value, allow us to see how the MNP distribution changes along *x* and *y* axis in the areas where they are present in greater amounts. Fig 11c shows that MNP are distributed almost homogeneously in the sample $1A$, but they are in a limited part of the scaffold. Conversely, the figure 12c referring to the sample 2A, shows a larger presence of MNPs in the central region (*x* ranging from 1.5 to 3 mm and *y* between 1 and 3.5 mm). Sample $3A$ (see Fig. 13c), which contains the largest amount of MNPs, has a homogeneous distribution along the *x* and *y* axes like sample $1A$, and in this case MNP fill almost the entire scaffold.

VII. Conclusion

This paper has proposed a strategy exploiting THz technology for non-destructive inspection of composite materials, especially MagS which are used in various biomedical applications.

The presented approach allows a quantitative characterization providing an estimate of the thickness (Δ) and refractive index (η) of the MagS. In addiction, two reference propagation time are introduced. The procedure allows us to define two indices, the magnetization index, I_m, and the magnetization distribution index, I_{md}, which take into account the areas where MNPs occur and give us information about the region where they are present in greater quantities, respectively.
It is worth noting that THz imaging enables non-destructive characterization without the use of ionizing radiation, as in MicroCTs, and with a less complex and laborious measurement procedure (i.e., the samples are simply placed on the scanning area of the THz system) compared to other techniques such as SEM and TEM. Furthermore, unlike other non-destructive techniques, THz ToF imaging has the advantage of allowing a 3D characterization of the object under test.

To the best of our knowledge, this paper presents a novel method based on the use of THz non-destructive characterization of MagS used for biomedical applications. The proposed approaches and our results could be relevant to materials scientists, bioengineers and clinicians who want to fabricate, characterize and use MagS as multifunctional tools for tissue engineering, drug delivery and hyperthermia. The results presented in this paper support the possibility of using THz technology to improve MagS fabrication techniques. The study addressed in this paper opens new challenges aimed at 3D characterization of the MagS (i.e., evaluation of the volumetric distribution of the MNPs in the scaffold) which would allow estimation of the concentration of the MNPs in the polymer matrix.

Acknowledgments

This work has been partially supported by PRIN BEST-Food – Broadband Electromagnetic Sensing Technologies for Food quality and security assessment-B64I19001250001.

References

[1] Mel M Schwartz, "Composite materials handbook," 1983.
[2] Pankaj K Mallick, *Composites engineering handbook*, CRC Press, 1997.
[3] Robert M Jones, "Taylor and francis,"," *Mechanics of Composite Materials*, 1999.
[4] Alexander E Bogdanovich and Robert L Sierakowski, "Composite materials and structures: Science, technology and applications-a compendium of books, review papers, and other sources of information," 1999.
[5] I Amenabar, F Lopez, and A Mendikute, "In introductory review to THz non-destructive testing of composite mater," *Journal of Infrared, Millimeter, and Terahertz Waves*, vol. 34, no. 2, pp. 152–169, 2013.
[6] V Antonucci, M Giordano, L Nicolais, A Calabro, A Cusano, A Cutolo, and S Inserra, "Resin flow monitoring in resin film infusion process," *Journal of Materials Processing Technology*, vol. 143, pp. 687–692, 2003.
[7] S Bickerton, EM Sozer, P Šimácek, and SG Advani, "Fabric structure and mold curvature effects on preform permeability and mold filling in the rtm process. part ii. predictions and comparisons with experiments," *Composites Part A: Applied Science and Manufacturing*, vol. 31, no. 5, pp. 439–458, 2000.
[8] B Qi, J Raju, T Kruckenberg, and R Stanning, "A resin film infusion process for manufacture of advanced composite structures," *Composite structures*, vol. 47, no. 1-4, pp. 471–476, 1999.
[9] Paula IP Soares, Joana Romão, Ricardo Matos, Jorge Carvalho Silva, and João Paulo Borges, "Design and engineering of magneto-responsive devices for cancer theranostics: Nano to macro perspective," *Progress in Materials Science*, vol. 116, pp. 100742, 2021.
[10] Omid Sedighi, Amirhossein Alaghmandfard, Maziar Montazerian, and Francesco Baino, "A critical review of bioceramics for magnetic hyperthermia," *Journal of the American Ceramic Society*, vol. 105, no. 3, pp. 1723–1747, 2022.
[11] Matteo Bruno Lodi, Alessandro Fanti, Andrea Vargiu, Maurizio Bozzi, and Giuseppe Mazzarella, "A multiphysics model for bone repair using magnetic scaffolds for targeted drug delivery," *IEEE Journal on Multiscale and Multiphysics Computational Techniques*, vol. 6, pp. 201–213, 2021.
[12] Silke Behrens, "Preparation of functional magnetic nanocomposites and hybrid materials: recent progress and future directions," *Nanoscale*, vol. 3, no. 3, pp. 877–892, 2011.
[13] Simone Sprio, Elisabetta Campodoni, Monica Sandri, Lorenzo Preti, Tobias Keppler, Frank A Müller, Nicola M Pugno, and Anna Tampieri, "A graded multifunctional hybrid scaffold with superparamagnetic ability for periodontal regeneration," *International journal of molecular sciences*, vol. 19, no. 11, pp. 3604, 2018.
[14] Yuhui Li, Guoyou Huang, Xiaohui Zhang, Baoqiang Li, Yongmei Chen, Tingli Lu, Tian Jian Lu, and Feng Xu, "Magnetic hydrogels and their potential biomedical applications," *Advanced Functional Materials*, vol. 23, no. 6, pp. 660–672, 2013.
[15] Song Li, Changling Wei, and Yonggang Lv, "Preparation and application of magnetic responsive materials in bone tissue engineering," *Current Stem Cell Research & Therapy*, vol. 15, no. 5, pp. 428–440, 2020.
[16] Alessandro Russo, Michele Bianchi, M Sartori, Marco Boi, G Giavaresi, DM Salter, Mislav Jelic, Maria Cristina Maltarello, A Ortolani, S Sprio, et al., "Bone regeneration in a rabbit critical femoral defect by means of magnetic hydroxyapatite macroporous scaffolds," *Journal of Biomedical Materials Research Part B: Applied Biomaterials*, vol. 106, no. 2, pp. 546–554, 2018.
[17] Jianghong Huang, Wei Liu, Yujie Liang, Long Li, Li Duan, Jielin Chen, Feiyan Zhu, Yuxiao Lai, Weimin Zhu, Wei You, et al., "Preparation and biocompatibility of diphasic magnetic nanocomposite scaffold," *Materials Science and Engineering: C*, vol. 87, pp. 70–77, 2018.
[18] Yao Zhao, Tiantang Fan, Jingdi Chen, Jiacan Su, Xin Zhi, Panpan Pan, Lin Zou, and Qiqing Zhang, "Magnetic bioinspired micro/nanostructured composite scaffold for bone regeneration," *Colloids and Surfaces B: Biointerfaces*, vol. 174, pp. 70–79, 2019.
[19] Matteo Bruno Lodi, Alessandro Fanti, Giacomo Muntoni, and Giuseppe Mazzarella, "A multiphysic model for the hyperthermia treatment of residual osteosarcoma cells in upper limbs using magnetic scaffolds," *IEEE Journal on Multiscale and Multiphysics Computational Techniques*, vol. 4, pp. 337–347, 2019.
[20] R De Santis, A Gloria, T Russo, U d'Amora, S Zeppetelli, C Dionigi, A Sytcheva, T Herrmannsdörfer, V Dediu, and L Ambrosio, "A basic approach toward the development of nanocomposite magnetic scaffolds for advanced bone tissue engineering," *Journal of Applied Polymer Science*, vol. 122, no. 6, pp. 3599–3605, 2011.

[21] M Bañobre-López, Y Piñeiro-Redondo, R De Santis, A Gloria, L Ambrosio, Anna Tampieri, V Dediu, and J Rivas, "Poly (caprolactone) based magnetic scaffolds for bone tissue engineering," *Journal of applied physics*, vol. 109, no. 7, pp. 07B313, 2011.

[22] Jung-Ju Kim, Rajendra K Singh, Seog-Jin Seo, Tae-Hyun Kim, Joong-Hyun Kim, Eun-Jung Lee, and Hae-Won Kim, "Magnetic scaffolds of polycaprolactone with functionalized magnetite nanoparticles: physicochemical, mechanical, and biological properties effective for bone regeneration," *Rsc Advances*, vol. 4, no. 33, pp. 17325–17336, 2014.

[23] Azam Hajinasab, Saeed Saber-Samandari, Sara Ahmadi, and Kadhim Alamara, "Preparation and characterization of a biocompatible magnetic scaffold for biomedical engineering," *Materials Chemistry and Physics*, vol. 204, pp. 378–387, 2018.

[24] Aaron C Small and James H Johnston, "Novel hybrid materials of magnetic nanoparticles and cellulose fibers," *Journal of Colloid and Interface Science*, vol. 331, no. 1, pp. 122–126, 2009.

[25] Hyung-Mun Yun, Su-Jin Ahn, Kyung-Ran Park, Mi-Joo Kim, Jung-Ju Kim, Guang-Zhen Jin, Hae-Won Kim, and Eun-Cheol Kim, "Magnetic nanocomposite scaffolds combined with static magnetic field in the stimulation of osteoblastic differentiation and bone formation," *Biomaterials*, vol. 85, pp. 88–98, 2016.

[26] Hadas Skaat, Ofra Ziv-Polat, Abraham Shahar, David Last, Yael Mardor, and Shlomo Margel, "Magnetic scaffolds enriched with bioactive nanoparticles for tissue engineering," *Advanced healthcare materials*, vol. 1, no. 2, pp. 168–171, 2012.

[27] Claire Gervais, Mathieu Thoury, Solenn Réguer, Pierre Gueriau, and Jennifer Mass, "Radiation damages during synchrotron x-ray microanalyses of prussian blue and zinc white historic paintings: detection, mitigation and integration," *Applied Physics A*, vol. 121, no. 3, pp. 949–955, 2015.

[28] P Sivakumar, R Ramesh, A Ramanand, S Ponnusamy, and C Muthamizhchelvan, "Synthesis and characterization of nickel ferrite magnetic nanoparticles," *Materials Research Bulletin*, vol. 46, no. 12, pp. 2208–2211, 2011.

[29] Vijaya Barge, Pranali Yendhe, Kavita Kodre, Sneha Attarde, and Ravindra Patil, "Electron microscopy: A review," 2014.

[30] Anjali Priya, Abhishek Singh, and Nikhil Anand Srivastava, "Electron microscopy–an overview," *International Journal of Students' Research in Technology & Management*, vol. 5, no. 4, pp. 81–87, 2017.

[31] S Wietzke, C Jansen, M Reuter, T Jung, D Kraft, S Chatterjee, BM Fischer, and M Koch, "Terahertz spectroscopy on polymers: A review of morphological studies," *Journal of Molecular Structure*, vol. 1006, no. 1-3, pp. 41–51, 2011.

[32] Zachary D Taylor, Rahul S Singh, David B Bennett, Priyamvada Tewari, Colin P Kealey, Neha Bajwa, Martin O Culjat, Alexander Stojadinovic, Hua Lee, Jean-Pierre Hubschman, et al., "THz medical imaging: in vivo hydration sensing," *IEEE transactions on science and technology*, vol. 1, no. 1, pp. 201–219, 2011.

[33] Katsuhiro Ajito, "Terahertz spectroscopy for pharmaceutical and biomedical applications," *IEEE Transactions on Terahertz Science and Technology*, vol. 5, no. 6, pp. 1140–1145, 2015.

[34] Richard Knipper, Anika Brahm, Erik Heinz, Torsten May, Gunther Notni, Hans-Georg Meyer, Andreas Tünnermann, and Jürgen Popp, "THz absorption in fabric and its impact on body scanning for security application," *IEEE Transactions on Terahertz Science and Technology*, vol. 5, no. 6, pp. 999–1004, 2015.

[35] Ilaria Catapano and Francesco Soldovieri, "A data processing chain for terahertz imaging and its use in artwork diagnostics," *Journal of Infrared, Millimeter, and Terahertz Waves*, vol. 38, no. 4, pp. 518–530, 2017.

[36] Sonia Zappia, Lorenzo Crocco, and Ilaria Catapano, "THz imaging for food inspections: A technology review and future trends," *Terahertz Technology*, 2021.

[37] Egor V Yakovlev, Kirill I Zaytsev, Irina N Dolganova, and Stanislav O Yurchenko, "Non-destructive evaluation of polymer composite materials at the manufacturing stage using terahertz pulsed spectroscopy," *IEEE Transactions on Terahertz science and Technology*, vol. 5, no. 5, pp. 810–816, 2015.

[38] Yun-Shik Lee, *Principles of terahertz science and technology*, vol. 170, Springer Science & Business Media, 2009.

[39] Jose A Hejase, Pavel R Paladhi, and Premjeet Prem Chahal, "Terahertz characterization of dielectric substrates for component design and nondestructive evaluation of packages," *IEEE Transactions on Components, Packaging and Manufacturing Technology*, vol. 1, no. 11, pp. 1685–1694, 2011.

[40] Liang Cheng and Gui Yun Tian, "Comparison of nondestructive testing methods on detection of delaminations in composites," *Journal of sensors*, vol. 2012, 2012.

[41] Robert Bogue, "New ndt techniques for new materials and applications," *Assembly Automation*, 2012.

[42] Przemyslaw Lopato and Tomasz Chady, "Time reversal pulsed terahertz inspection of dielectric structures," *International Journal of Applied Electromagnetics and Mechanics*, vol. 39, no. 1-4, pp. 427–433, 2012.

[43] David Kuei Hsu, Kil-Sung Lee, Je-Woong Park, Yong-Deuck Woo, and Kwang-Hee Im, "Nde inspection of terahertz waves in wind turbine composites," *International journal of precision engineering and manufacturing*, vol. 13, no. 7, pp. 1183–1189, 2012.

[44] Frank Ospald, Wissem Zouaghi, René Beigang, Carsten Matheis, Joachim Jonuscheit, Benoit Recur, Jean-Paul Guillet, Patrick Mounaix, Wouter Vleugels, Pablo Venegas Bosom, et al., "Aeronautics composite material inspection with a terahertz time-domain spectroscopy system," *Optical Engineering*, vol. 53, no. 3, pp. 031208, 2013.

[45] Edison Cristofani, Fabian Friederich, Sabine Wohnsiedler, Carsten Matheis, Joachim Jonuscheit, Marijke Vandewal, and René Beigang, "Nondestructive testing potential evaluation of a terahertz frequency-modulated continuous-wave imager for composite materials inspection," *Optical Engineering*, vol. 53, no. 3, pp. 031211, 2014.

[46] Bernd M Fischer, Steffen Wietzke, Marco Reuter, Ole Peters, Ralf Gente, Christian Jansen, Nico Vieweg, and Martin Koch, "Investigating material characteristics and morphology of polymers using terahertz technologies," *IEEE Transactions on Terahertz Science and Technology*, vol. 3, no. 3, pp. 259–268, 2013.

[47] Melissa L Mather, Stephen P Morgan, Lisa J White, Hongyun Tai, Walter Kockenberger, Steven M Howdle, Kevin M Shakesheff, and John A Crowe, "Image-based characterization of foamed polymeric tissue scaffolds," *Biomedical materials*, vol. 3, no. 1, pp. 015011, 2008.

[48] Frank Rutz, Martin Koch, Shilpa Khare, Martin Moneke, Heike Richter, and Uwe Ewert, "Terahertz quality control of polymeric products," *International Journal of Infrared and Millimeter Waves*, vol. 27, no. 4, pp. 547–556, 2006.

[49] S Wietzke, C Jansen, C Jördens, N Krumbholz, N Vieweg, M Scheller, MK Shakfa, D Romeike, T Hochrein, M Mikulics, et al., "Industrial applications of THz systems," in *International Symposium on Photoelectronic Detection and Imaging 2009: Terahertz and High Energy Radiation Detection Technologies and Applications*. International Society for Optics and Photonics, 2009, vol. 7385, p. 738506.

[50] Fabien Destic and Christophe Bouvet, "Impact damages detection on composite materials by THz imaging," *Case studies in nondestructive testing and evaluation*, vol. 6, pp. 53–62, 2016.

[51] Egor V Yakovlev, Kirill I Zaytsev, Irina N Fokina, Valeriy E Karasik, and Stanislav O Yurchenko, "Nondestructive testing of polymer composite materials using THz radiation," in *Journal of Physics: Conference Series*. IOP Publishing, 2014, vol. 486, p. 012008.

[52] Matteo Bruno Lodi, Nicola Curreli, Sonia Zappia, Luca Pilia, Maria Francesca Casula, Sergio Fiorito, Ilaria Catapano, Francesco Desogus, Teresa Pellegrino, Ilka Kriegel, et al., "Influence of magnetic scaffold loading patterns on their hyperthermic potential against bone tumors," *IEEE transactions on bio-medical engineering*, 2021.

[53] S Zappia, I Catapano, R Scapaticci, MB Lodi, A Fanti, and L Crocco, "Magnetic nanoparticles distribution estimate in polymeric scaffolds using THz imaging," in *proceeding of 2022 XXIV National Meeting of Electromagnetics (Rinem 2022), Catania (Italy), September 2022*.

[54] S Zappia, L Crocco, R Scapaticci, MB Lodi, A Fanti, and I Catapano, "Terahertz imaging of magnetic scaffolds," in *proceeding of VI National Conference "Interaction between electromagnetic fields and biosystems (ICEmB 2022), Cagliari (Italy), July 2022*.

[55] Brahatheeswaran Dhandayuthapani, Yasuhiko Yoshida, Toru Maekawa, and D Sakthi Kumar, "Polymeric scaffolds in tissue engineering application: a review," *International journal of polymer science*, vol. 2011, 2011.

[56] Lisa E Freed and Gordana Vunjak-Novakovic, "Culture of organized cell communities," *Advanced drug delivery reviews*, vol. 33, no. 1-2, pp. 15–30, 1998.

[57] Vassilis Karageorgiou and David Kaplan, "Porosity of 3d biomaterial scaffolds and osteogenesis," *Biomaterials*, vol. 26, no. 27, pp. 5474–5491, 2005.

[58] Jun Takayanagi, Hiroki Jinno, Shingo Ichino, Koji Suizu, Masatsugu Yamashita, Toshihiko Ouchi, Shintaro Kasai, Hideyuki Ohtake, Hirohisa Uchida, Norihiko Nishizawa, et al., "High-resolution time-of-flight terahertz tomography using a femtosecond fiber laser," *Optics express*, vol. 17, no. 9, pp. 7533–7539, 2009.

[59] Daniel M Mittleman, Rune H Jacobsen, and Martin C Nuss, "T-ray imaging," *IEEE Journal of selected topics in quantum electronics*, vol. 2, no. 3, pp. 679–692, 1996.
[60] Ilaria Catapano, Antonio Affinito, Luigi Guerriero, Bruno Bisceglia, and Francesco Soldovieri, "Majolica imaging with THz waves: preliminary results," *Applied Physics A*, vol. 122, no. 5, pp. 533, 2016.
[61] Michael Panzner, Udo Klotzbach, Eckhard Beyer, Frank Rutz, Christian Jördens, and Martin Koch, "Non-destructive investigation of paintings with THz-radiation," 2006.
[62] Konstantinos Konstantinides, Balas Natarajan, and Gregory S Yovanof, "Noise estimation and filtering using block-based singular value decomposition," *IEEE transactions on image processing*, vol. 6, no. 3, pp. 479–483, 1997.

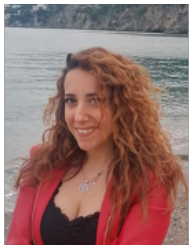

Sonia Zappia received the master's degree in biomedical engineering from "Federico II" University of Naples, Naples, Italy, in 2019, where she is currently pursuing the Ph.D. degree with the Department of Electrical Engineering and Information Technology. In 2019, she was with the Regional Center Information Communication Technology (CeRICT), Naples, Italy. From 2020 she has been working at the Institute of Electromagnetic Sensing of the Environment, National Research Council of Italy (IREA-CNR), Naples, Italy, as a Research Fellow. Her research activity involves imaging with terahertz (THz) time-domain signals and THz spectroscopy.

Rosa Scapaticci (Member, IEEE) received the M.S. Laurea degree (summa cum laude) in biomedical engineering from "Federico II" University of Naples, Naples, Italy, in 2010 and the Ph.D. degree in Information Engineering from "Mediterranea" University of Reggio Calabria, Reggio Calabria, Italy, in 2014. From December 2013 she has been working at the Institute of Electromagnetic Sensing of the Environment, National Research Council of Italy (IREA-CNR), Naples, Italy, first as a Research Fellow and from September 2017 as a Researcher. Her scientific interests include electromagnetic scattering problems, imaging methods for noninvasive diagnostics and they are mainly focused on the development of innovative microwave imaging approaches in the framework of biomedical applications, as well as therapeutic applications of electromagnetic fields. Dr. Scapaticci is co-author of more than 90 papers on international journals and conference proceedings. In 2013, she received the best Student Member Paper Award from the IEEE Antennas and Propagation Society Central and Southern Italy Chapter. She received from the Italian Society of Electromagnetics, the Barzilai Award and the Latmiral Award in September 2014 and in September 2018, respectively.

Matteo B. Lodi (Member, IEEE) received the Bachelor's degree in Biomedical Engineering from the University of Cagliari, Cagliari, in 2016, and the Master's degree in Biomedical Engineering from Politecnico di Torino, Turin, Italy, in 2018. In 2022 he received, with honour, the PhD in Electronic Engineering and Computer Science, from the University of Cagliari. He is currently working as technologist in the Applied Electromagnetics Group at the University of Cagliari. His research activity deals with the modelling of bioelectromagnetic phenomena, especially hyperthermia treatment; the study, manufacturing, and synthesis of magnetic biomaterials for tissue engineering applications; and the use of microwaves for biotechnology and environmental applications, while working in the design and characterization of antennas for sapace and wearable applications. He has been awarded as Young Scientists at the General Assembly and Scientific Symposium of URSI in 2020 and 2021. In 2019 he received the Best Poster Award at IX International School of Bioelectromagnetism "Alessandro Chiabrera" and in 2021 he was a co-author of the "2021 IEEE IST Best Student Paper Award" at IEEE International Conference on Imaging Systems & Techniques.

Alessandro Fanti (Senior Member, IEEE) received the Laurea degree in electronic engineering and the Ph.D. degree in electronic engineering and computer science from the University of Cagliari, Cagliari, Italy, in 2006 and 2012, respectively. From 2013 to 2016, he was a Postdoctoral Fellow of the Electromagnetic Group, University of Cagliari, where he is currently an Assistant Professor. He has authored or coauthored 57 papers in international journals. His research interests include the use of numerical techniques for modes computation of guiding structures, optimization techniques, analysis and design of waveguide slot arrays, analysis and design of patch antennas, radio propagation in urban environment, modeling of bioelectromagnetic phenomena, and microwave exposure systems for biotechnology and bioagriculture.

Giuseppe Ruello (Senior Member, IEEE) was born in Naples, Italy, in 1975. He received the Laurea degree (cum laude) in telecommunication engineering and the Ph.D. degree in information engineering from the University of Naples Federico II, Naples, in 1999 and 2003, respectively. In 2002 and from 2004 to 2005, he was a Visiting Scientist with the Department of Signal Theory and Communications, Universitat Politecnica de Catalunya, Barcelona, Spain. He is currently a tenure-track Assistant Professor of Electromagnetics with the Department of Electrical Engineering and Information Technology, University of Naples Federico II. His research interests include synthetic aperture radar (SAR) remote sensing, modeling of electromagnetic scattering from natural surfaces, fractal models, SAR raw signal simulation, modeling of electromagnetic field propagation in urban environment, and remote sensing techniques for low-income semiarid regions.

Lorenzo Crocco (Senior Member, IEEE) is a Senior Researcher with the Institute for the Electromagnetic Sensing of the Environment, National Research Council of Italy (IREA-CNR). His scientific activities mainly concern electromagnetic scattering, with a focus on diagnostic and therapeutic uses of EM fields, through-the-wall radar and GPR. On these topics, he has published more than 100 papers, given keynote talks and led or participated to research projects. From 2013 he is Italian representative in the Management Committees of COST actions devoted to medical applications of EM fields (MiMed on microwave imaging and MyWAVE on therapeutic applications of electromagnetic waves). Since 2017, he is Member of the Board of Directors of the Italian Electromagnetic Society (SIEm). Since 2019, he is a member of the Italian URSI Commission. In 2019, he has been elected in the Scientific Board of the Engineering Department (DIITET) of CNR. Dr. Crocco has been the recipient of the SIEm "Barzilai" Award for Young Scientists (2004) and YSA at the URSI General Assembly held in New Delhi (India) in 2005.

Ilaria Catapano (Member, IEEE) received the Ph.D. degree in electric and information engineering from the University of Cassino, Cassino, Italy, in 2006. In 2003, in the framework of her Ph.D. project, she started her research activity with the Institute for Electromagnetic Sensing of the Environment, National Research Council of Italy (IREA-CNR), Naples, Italy, where she is a Senior Researcher. Her research activities deal with noninvasive electromagnetic diagnostics and are mainly focused on models and strategies for electromagnetic forward and inverse scattering problems, development and performance assessment of microwave imaging approaches for shape reconstruction, processing of experimental data gathered by radar systems for subsurface surveys, and THz spectroscopy and imaging. Dr. Catapano has co-authored over 150 articles, mainly in scientific journals or proceedings of international conferences. She received the G. Barzilai Award from the Italian Electromagnetic Society in 2004; she was one of the young scientist awardees at the XXIX URSI General Assembly in 2008.